Diurnal Coupling in the Tropical Oceans of CCSM3

Gokhan Danabasoglu, William G. Large, Joseph J. Tribbia, Peter R. Gent, and
Bruce P. Briegleb

National Center for Atmospheric Research,* Boulder, Colorado

James C. McWilliams

National Center for Atmospheric Research, Boulder, Colorado, and Department of Atmospheric Sciences, and Institute of
Geophysics and Planetary Physics, University of California, Los Angeles, Los Angeles, California*

ABSTRACT

New features that may affect the behavior of the upper ocean in the Community Climate System Model version 3 (CCSM3) are described. In particular, the addition of an idealized diurnal cycle of solar forcing where the daily mean solar radiation received in each daily coupling interval is distributed over 12 daylight hours is evaluated. The motivation for this simple diurnal cycle is to improve the behavior of the upper ocean, relative to the constant forcing over each day of previous CCSM versions. Both 1- and 3-h coupling intervals are also considered as possible alternatives that explicitly resolve the diurnal cycle of solar forcing. The most prominent and robust effects of all these diurnal cycles are found in the tropical oceans, especially in the Pacific. Here, the mean equatorial sea surface temperature (SST) is warmed by as much as 1°C, in better agreement with observations, and the mean boundary layer depth is reduced. Simple rectification of the diurnal cycle explains about half of the shallowing, but less than 0.1°C of the warming. The atmospheric response to prescribed warm SST anomalies of about 1°C displays a very different heat flux signature. The implication, yet to be verified, is that large-scale air–sea coupling is a prime mechanism for amplifying the rectified, daily averaged SST signals seen by the atmosphere. Although the use of upper-layer temperature for SST in CCSM3 underestimates the diurnal cycle of SST, many of the essential characteristics of diurnal cycling within the equatorial ocean are reproduced, including boundary layer depth, currents, and the parameterized vertical heat and momentum fluxes associated with deep-cycle turbulence. The conclusion is that the implementation of an idealized diurnal cycle of solar forcing may make more frequent ocean coupling and its computational complications unnecessary as improvements to the air–sea coupling in CCSM3 continue. A caveat here is that more frequent ocean coupling tends to reduce the long-term cooling trends typical of CCSM3 by heating already too warm ocean depths, but longer integrations are needed to determine robust features. A clear result is that the absence of diurnal solar forcing of the ocean has several undesirable consequences in CCSM3, including too large ENSO variability, much too cold Pacific equatorial SST, and no deep-cycle turbulence.

1. Introduction

The atmosphere and ocean continuously exchange momentum, heat, freshwater, and various passive tracers, but there are fundamental reasons why this cannot be properly represented in numerical models of the coupled system, on any scale. Obviously, the time discretization of the conservation equations implicitly inhibits flux variability over a time step. In this regard, the best possible scheme would be to have equal ocean and atmosphere time steps, with an atmospheric radiation calculation each time. However, this would have serious practical implications for the numerics and computational expense. In addition, the uncertainty in computed air–sea fluxes grows as the time and space scales get smaller, though a quantitative assessment is hindered by the lack of direct ocean flux observations, such as provided by a drag plate (Bradley 1968) over some land surfaces. Another issue is that the transfer coeffi-

cients used to calculate the turbulent fluxes of momentum, sensible heat, and evaporation are determined empirically from measurements averaged over about an hour (e.g., Large and Pond 1981) and may not be applicable for instantaneous output from an atmospheric model grid point. Also, they are not often formulated to account for real variations in wind/wave conditions that occur over the 3–7-day synoptic period (see Brunke et al. 2002). In principle, the coupled system could include a surface wave model (Komen et al. 1994) to support such formulations (e.g., Bourassa et al. 1999), but the gain versus cost has not been established.

The diurnal cycle of solar radiation produces large changes in land surface temperatures (tens of °C) and the surface temperature of a sea ice model. These changes have an order-one effect on atmospheric stability and need to be temporally resolved in a coupled model. Sea surface temperatures (SSTs), however, exhibit a much smaller diurnal cycle, because of the large heat capacity of seawater, significant solar radiation penetration below the surface, and the turbulent vertical mixing. Sometimes other factors, such as a net surface cooling during the day, or the mixing of cold water from below, or frontal passages, dominate, and SST is not always greater during the day than the previous night. However, in conditions of very low wind and very large solar heating, the stabilizing heating can overcome the destabilizing wind mixing, such that diurnal solar heating is confined within the upper few meters of the ocean until nighttime convection mixes it deeper. The net result is a diurnal cycle of both mixed layer depth and SST, where the latter can exceed 2°C peak to peak even in the subtropics (Briscoe and Weller 1984).

Diurnal cycles of SST greater than 2°C have also been reported from the western warm pool of the equatorial Pacific (e.g., Fairall et al. 1996a; Anderson et al. 1996) and are expected across the equatorial Atlantic where low winds are even more frequent. East of the date line in the Pacific cold tongue, low winds are less frequent, so the diurnal cycle of SST is not expected to often exceed 1°C peak to peak (Webster et al. 1996). Nevertheless, Deser and Smith (1998) suggest that this signal is sufficient to contribute to an observed, zonally symmetric diurnal cycle in equatorial wind divergence that arises from an out-of-phase relationship between diurnal variability in meridional winds across the equator. At high latitudes, the satellite-based estimates suggest predominantly lower SST diurnal cycle magnitudes (Kawai and Kawamura 2002; Stuart-Menteth et al. 2003). An atmospheric general circulation model's response to such small signals is expected to be very weak as documented in Magnusdottir et al. (2004) for much larger (several degrees Celsius) North Atlantic SST anomalies.

Ocean observations on the equator at 140°W show mixed layer depth excursions from more than 60 m at night to less than 10 m during day (Lien et al. 1995). Companion measurements of turbulent dissipation also display an unexpectedly strong diurnal modulation below the mixed layer (Gregg et al. 1985; Moum and Caldwell 1985). Between the mixed layer and core of the Equatorial Undercurrent (EUC), this deep-cycle turbulence is characterized by a late-night to early-morning maximum in dissipation that is as much as 100 times greater than 12 h before or after (Lien et al. 1995), with the peak occurring at deeper depths at later times. The essential characteristics have been reproduced in large-eddy simulations (LESs; Wang et al. 1998; Skyllingstad et al. 1999) and one-dimensional models of parameterized mixing (Schudlich and Price 1992; Large and Gent 1999).

The primary goal of this work is to evaluate, from an oceanic viewpoint, one aspect of the standard air–sea coupling implemented in the Community Climate System Model version 3 (CCSM3), relative to possible alternatives. This particular issue is the change, since the release of CCSM2 (Kiehl and Gent 2004), in how daily mean solar radiation is distributed in time as ocean forcing. A secondary purpose is to document the specific ocean model implementation, especially two other important model developments that affect upper-ocean behavior. Specifically, these are modifications to the Large et al. (1994) K-Profile Parameterization (KPP; appendix A) and implementation of spatially varying monthly solar absorption based on ocean color observations (appendix B). The coupling details, including the distribution of solar radiation according to an idealized diurnal cycle, and the relevant CCSM3 ocean and atmospheric model physics are presented in section 2. In section 3, the ocean model is summarized, and the numerical experiments are described. The main results, concerning coupled ocean model drift, ocean mean state, equatorial diurnal rectification, deep-cycle turbulence, role of the atmospheric mean state, and ENSO variability, are presented in sections 4 through 9, respectively.

2. Air–sea coupling in CCSM3

In this study, CCSM3 refers to the T85×1 configuration where a T85 spectral truncation (1.4° × 1.4° horizontal transform grid), 26-level atmosphere [Community Atmospheric Model version 3 (CAM3); Collins et al. 2006a] is coupled to a nominal 1°, 40-level ocean (see section 3). The land component grid matches the atmo-

sphere, and the sea ice shares the ocean model's horizontal grid. Further details of the overall configuration are given in Collins et al. (2006b).

The flux calculations and property exchanges, including the treatment of differing horizontal grids and sea ice, are detailed in Bryan et al. (1996), where the bulk formulas given in Large et al. (1994) are used. These formulas are also given in Brunke et al. (2002), who show that they are generally consistent with alternatives such as the Coupled Ocean–Atmosphere Response Experiment (COARE) algorithm (Fairall et al. 1996b). They are preferred even to the more recent COARE3 algorithm (Fairall et al. 2003), because measurements from a larger range of wind speeds (from 1 m s^{-1} to more than 25 m s^{-1}) and from more stable atmospheric conditions were utilized in their formulation. However, a feature of fully coupled models is that this choice is not critical, because the surface fluxes are largely determined by other factors. For example, the surface stress substantially depends on the eddy momentum flux convergence aloft in the atmospheric model.

A more important issue is that these calculations use the ocean upper-level temperature, T_1, and current $\mathbf{V}_1$, together with the lowest-level (typically 60 m in CAM3) atmospheric wind, temperature, and humidity. At best these ocean values represent the ocean at half the upper-layer thickness (5 m in CCSM3) and are a poor approximation of the surface in low wind and strong solar heating situations. The use of the atmospheric state at 60 m becomes problematic in shallow boundary layers where the stability-modified logarithmic profiles are not valid up to such a height. These profiles are assumed in the iterative procedure (Large and Yeager 2004) used to shift the bulk transfer coefficients up from the standard 10-m height where they are formulated. Such boundary layers are found in light winds and very stable conditions.

The solar cycle is by far the most dominant diurnal signal, so the ocean errors arising from the CCSM3 flux calculations on these time scales should be relatively small, as shown by the following. A rough estimate of the change in heat flux into the ocean, ΔQ (in W m^{-2}), expected from a change in SST, ΔSST (in °C), is given by

$$\Delta Q = -0.4[C_{LW} + U(1.4 + C_{LH})]\Delta SST, \quad (1)$$

for a wind speed U in m s^{-1}. Differentiation of the bulk formulas for sensible and latent heat with respect to SST gives the 1.4 U and C_{LH} U terms, respectively, while C_{LW} comes from the outgoing longwave radiation. Doney et al. (1998) find that the 0.4 factor crudely accounts for the heating and moistening of the near-

surface atmosphere in a fully coupled model. The dependency on SST can be accounted for with $C_{LW} = 4.6$, 5.4, and 6.3 and $C_{LH} = 0.9$, 2.7, and 4.5 at SST = 0°, 15°, 30°C. According to WGASF (2000), the use of T_1, which neglects diurnal cool-skin and warm-layer temperature effects (Fairall et al. 1996a), should not be a serious problem for mean flux determinations. To illustrate, consider the extreme case where T_1 underestimates the diurnal cycle of SST by 2°C with a 2 m s^{-1} wind and SST = 30°C. The heat flux error from (1) is $\Delta Q = -14$ W m^{-2}. The mean flux difference over a day would be less than half this amount and well within the combined uncertainties arising from other issues such as the short-term accuracy of bulk formulas, and the use of atmospheric variables from 60-m height in light winds. Such days are not common, so the effect on annual-mean and global heat fluxes is even less. Furthermore, a 2°C diurnal cycle with 2 m s^{-1} winds implies a peak solar heat flux of about 1000 W m^{-2} (Webster et al. 1996), so the relative contribution of the diurnal SST to the peak heat flux would be a less-than-2% reduction. This percentage cannot get much larger, because as weaker wind allows ΔSST to increase, U acts to reduce $|\Delta Q|$ in (1), and as the peak solar decreases, so does ΔSST, and hence $|\Delta Q|$.

Two important considerations of air–sea coupling in CCSM3 are the conservative exchange of properties between components (to minimize drift in long climate experiments without flux corrections) and simultaneous integration of the atmosphere and ocean models (for efficient use of some computer architectures). These considerations impact the flux calculations. Here, we present a brief summary of the time lag associated with these computations and refer to Bryan et al. (1996) and Kauffman et al. (2004) for details of how information propagates between the components of the coupled system. The ocean and atmosphere are integrated over an ocean coupling interval, N (a day in the standard CCSM3), as follows: Means over the previous interval, $N - 1$ (the previous day), are exchanged, with the ocean model sending its T_1 and $\mathbf{V}_1$, and receiving all the air–sea fluxes it needs to integrate over interval N. These fluxes are computed using hourly surface radiation and lowest-level atmospheric state along with the average T_1 and $\mathbf{V}_1$, from the preceding interval, $N - 2$ (two days before). A simple demonstration that the property exchanges are conservative is to ascribe the same calendar time (day) to the ocean N and atmosphere $N - 1$ intervals, so that over each time interval (day) both models are forced by the same fluxes.

Both physical and computational considerations support coupling less frequently than the CCSM3 atmospheric time step of 10 min, and running the ocean

model near its maximum possible time step of 1 h. The hourly radiation calculations, the use of bulk transfer coefficients, and the ocean time step sets the minimum sensible coupling frequency at 1 h. Less frequent coupling has some attractions, including less data transfer and more flexibility in the choices of component time steps. The latter stems from the desire to simplify the conservation of heat and salt by having the coupling interval be an exact multiple of both the ocean and atmospheric time steps. Another factor is that synchronization of the annual cycle of solar forcing throughout the coupled system is eased if year boundaries coincide with coupling intervals. These considerations led to the design of the standard CCSM3 with a 1-day coupling interval for the ocean model, while using 1-h coupling intervals for the other components of the coupled system.

Given this daily coupling, it is possible to improve the representation of ocean surface forcing in CCSM3, by distributing the daily net solar radiation, $\overline{Q}_s$, received from the coupler over an idealized diurnal cycle. Specifically, at every ocean model time step, the fraction of a day, t_D, is computed and the net solar radiation over the time step is given by

$$Q_s(t_D) = f(t_D)\overline{Q}_s, \tag{2}$$

where

$$f(t_D) = \begin{cases} 0, & \text{for} \quad 0 \leq t_D < 0.25 \quad \text{and} \quad 0.75 < t_D \leq 1.0; \\ 4\cos^2[(2t_D - 1)\pi], & \text{for} \quad 0.25 \leq t_D \leq 0.75. \end{cases} \tag{3}$$

The implementation of (2)–(3) precisely conserves the time integral of the shortwave heat flux over a day. The peak value of this idealized solar cycle is $4\,\overline{Q}_s$ at noon ($t_D = 0.5$). This simple, idealized formulation is geared toward the Tropics, where the diurnal cycle is the largest.

With this idealized solar forcing, more realistic representations of the diurnal cycle of mixed layer depth, SST, surface current, and equatorial deep-cycle turbulence are expected, because of comparisons of one-dimensional implementations of the vertical model physics (KPP) to LESs and observations (Large et al. 1994; Large and Gent 1999). The parameterized vertical mixing in the atmospheric boundary layer is similar (Holtslag and Boville 1993), but in CCSM3 it does not see any diurnal ocean variability.

3. Ocean model and numerical experiments

The ocean component of CCSM3 is a Bryan–Cox-type (Bryan 1969), level-coordinate model based on the Parallel Ocean Program (POP 1.4) of the Los Alamos National Laboratory (Smith et al. 1992; Dukowicz and Smith 1994; Smith et al. 1995). The model solves the primitive equations in general orthogonal coordinates in the horizontal subject to the hydrostatic and Boussinesq approximations. The barotropic equation is solved using a linearized, implicit free-surface formulation. This linearization assumption precludes the use of very thin (order a few meters) first-level thickness. The surface layer thickness may vary. However, because the freshwater fluxes are treated as virtual salt fluxes using a constant reference salinity, the global integral of the ocean volume does not change.

The ocean model has 320 (zonal) × 384 (meridional) × 40 (vertical) grid points, and it is referred to as x1ocn to reflect its nominal 1° horizontal resolution. The domain is global, including Hudson Bay, the Mediterranean Sea, and the Persian Gulf. The Bering Strait and Northwest passage are open to the Arctic Ocean. The grid is in spherical coordinates in the Southern Hemisphere. In the Northern Hemisphere, the grid North Pole is displaced into Greenland at 80°N and 40°W. The resolution is uniform at 1.125° in the zonal direction, but it varies considerably in the meridional direction. The finest meridional resolution occurs at the equator with 0.27°. It monotonically increases to about 0.53° at 32°S and stays constant farther south. In the Northern Hemisphere high latitudes, the minimum resolution is about 0.38° occurring in the northwestern Atlantic ocean, and the maximum resolution is about 0.64° located in the northwestern Pacific ocean. The vertical resolution is shown in Yeager et al. (2006). It monotonically increases from 10 to 250 m from the surface to a depth of about 2000 m, below which it remains uniform. The minimum ocean depth is 30 m and the maximum is 5500 m.

The Red, Baltic, Black, and Caspian Seas are unconnected marginal seas that receive zero freshwater flux, so that their average salinity (S) remains constant. The excess flux accumulated over each marginal sea is distributed as a surface flux over a neighboring ocean region; namely, the western Arabian Sea, the southeastern North Sea, eastern Mediterranean Sea, and the Barents–Kara Seas, respectively. Thus, these fluxes provide indirect connections to the global circulation. For example, the excess evaporation from the Red Sea

TABLE 1. List of numerical experiments. Ocean coupling is in hours; Δt represents the model tracer and momentum time steps in seconds; TS $(day)^{-1}$ is the number of full and half (averaging) time steps per calendar day.

Case	Ocean coupling (h)	Initial condition	End year	Δt (s)	TS $(day)^{-1}$ (full/half)
CCSM3	24 with Eqs. (2)–(3)	Levitus/rest	661	3600	23/2
C1D	24	Levitus/rest	99	3600	23/2
C3H	3	Year 50 of CCSM3	99	3086	24/8
C1H	1	Year 50 of CCSM3	99	1440	48/24

supplies salt to the surface of the Arabian Sea, and much of the large river runoff into the Baltic freshens the North Sea.

The Gent and McWilliams (1990) isopycnal transport parameterization with a mixing coefficient of 600 $m^2\,s^{-1}$ is used in the model tracer equations in its skew-flux form (Griffies 1998). The derivation assumes that the square of the isopycnal slope is small, so tapering of mixing coefficients is activated only for slopes greater than 0.3, rather than the more traditional 0.01. The momentum equations use the Large et al. (2001) anisotropic horizontal viscosity, as generalized by Smith and McWilliams (2003). The associated viscosity coefficients differ arbitrarily in the east–west and north–south directions. These two coefficients vary both spatially and temporally depending nonlinearly on the local deformation rate (Smagorinsky 1993), subject to a minimum value of 1000 $m^2\,s^{-1}$ and numerical constraints. The vertical mixing coefficients are determined using the KPP scheme of Large et al. (1994). As described in appendix A, we use a modified version that ameliorates a shallow bias in the boundary layer depths (HBL). In the ocean interior, the background internal wave mixing diffusivity varies in the vertical from $0.1 \times 10^{-4}\,m^2\,s^{-1}$ near the surface to $1.0 \times 10^{-4}\,m^2\,s^{-1}$ in the abyss. This increase occurs at about 1000-m depth, as a crude representation of the enhanced deep vertical mixing observed over rough topography (Ledwell et al. 2000). The vertical viscosity is everywhere a factor of 10 (the Prandtl number) larger. The updated double-diffusive mixing is given in appendix A. The solar absorption is specified by spatially varying global fields of monthly mean ocean surface chlorophyll concentration that were derived from satellite ocean color measurements and related to absorption coefficients (Ohlmann 2003; see appendix B). Further details of the ocean model physics and parameter choices can be found in Smith and Gent (2002).

In addition to the CCSM3 control, we consider 3 numerical experiments in this study (Table 1). In C1D, the ocean coupling remains at once a day, but no diurnal cycle effects are included. Like CCSM3, it is initialized with January-mean climatological potential temperature (θ) and S (Levitus et al. 1998; Steele et al. 2001

in the Arctic Ocean) and state of rest, but integrated only for 100 yr. In C1H and C3H, the ocean model is coupled every 1 and 3 h, respectively. They are initialized from year 50 of CCSM3 and integrated for 50 yr to year 100. Both of these cases resolve the diurnal solar cycle explicitly, and the feedback of the diurnal variations of SST on the atmospheric boundary layer is present, but the maximum heating at noon is artificially amplified by a few watts per meter squared, because the cold SSTs from 2 and 6 h earlier, respectively, underestimate the longwave, latent, and sensible cooling at this time of day. Because it has the highest frequency of coupling, C1H can be considered as the best representation of *truth*. Also, comparisons of C1H, C3H, and C1D solutions are used to document the effects of increased coupling frequency.

The ocean model uses the leapfrog time stepping scheme, and the associated time splitting error is eliminated using a time-averaging step. Without extensive code modifications, there needs to be at least one such averaging time step per ocean coupling interval. Therefore, more frequent coupling can require a larger number of both full and half (averaging) time steps per day (Table 1), such that C1H is about 3 times more expensive than CCSM3. C3H is a less expensive option that is used to determine if the results of C1H can be duplicated with less frequent coupling.

The analysis is confined to the 50-yr period covering model years 50–99. Unless otherwise noted, time-mean fields represent 20-yr averages for years 80–99. For the diurnal cycle analysis, a comprehensive set of output fields is obtained for every model time step (or every hour for C1H) for the first 5 days of all 12 months of a particular year. For this purpose, year 90 was chosen arbitrarily. Consequently, although their 20-yr means are very similar, the year 90 means somewhat differ between the diurnal cycle cases due to interannual variability.

4. Ocean drift

A 50-yr integration is obviously not long enough to determine the long-term behavior of the model solutions with great certainty, particularly in the abyssal

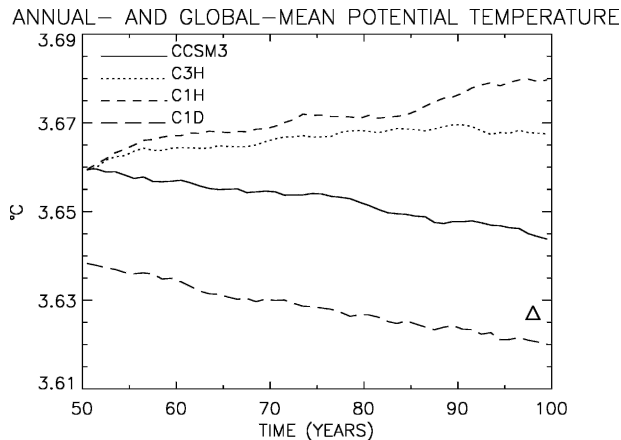ANNUAL– AND GLOBAL–MEAN POTENTIAL TEMPERATURE

FIG. 1. Annual- and global-mean potential temperature time series. The triangle denotes the climatological mean from observations (Levitus et al. 1998; Steele et al. 2001) computed on the model grid.

ocean and at high latitudes. The former is due to the slow diffusive processes, and the latter is largely due to both the storm track variability and long time scales associated with the sea ice. Nevertheless, because it exhibits important sensitivities to the coupling frequency, we first examine the ocean model drift.

The annual- and global-mean θ time series for years 50–99 are given in Fig. 1. Both CCSM3 and C1D lose heat at comparable rates (about -0.15 W m^{-2}, globally averaged) over the 50-yr period, indicating that the explicit diurnal cycle parameterization in CCSM3 does not affect the heat loss rate compared to omitting it. We note that both CCSM3 and C1D start from the same initial conditions (triangle in Fig. 1) and that C1D does not get as warm as CCSM3 during the first 40 yr (not shown) before they start cooling. In contrast, more frequent ocean coupling results in a reversal of the above cooling trends. Indeed, there is a monotonic increase in heat flux into the ocean from C1D to C1H, which has the largest warming trend with the most frequent coupling. We compute heat flux values of near 0 and +0.26 W m^{-2} for C3H and C1H, respectively, based on the θ trends between years 80–99.

The time- and horizontal-mean θ difference profiles for the three major basins and the globe are plotted in Fig. 2 to examine the vertical structure of the drifts in θ. These profiles are obtained by subtracting year 50 means from year 95–99 means for each case. Thus, the positive and negative values indicate warming and cooling trends, respectively, over this 50-yr period. For reference purposes, the CCSM3 year 50 profiles in comparison with the observed climatology are also included in the figure. Here, the southern boundaries of the basins extend to 34°S. The Labrador Sea and Greenland–

Iceland–Norwegian Seas are included in the Atlantic basin. Finally, all of the Indonesian Throughflow region south of 3°S and the region between Australia and New Guinea are included in the Indian Basin.

The global profiles show that the bulk of the warming in C3H and C1H occurs within the upper 1000 m, and the Pacific and Atlantic basins are the primary contributors. Consistent with Fig. 1, the upper-ocean warming is monotonically increasing with increased coupling frequency. This warming, however, represents a further degradation of already too warm (compared to observations) upper-ocean waters. The trends below 1500 m do not differ appreciably among cases because of the relatively short integration lengths. Here, the deep Atlantic and Pacific continue to get warmer and colder, respectively, at similar rates in all experiments, and there are virtually no trends below 3000 m in the Indian Ocean.

The time series of the annual- and global-mean S (not shown) display neither any significant trend differences between cases nor any monotonic behavior, in contrast with the θ time series. In fact, there are no appreciable global-mean S drifts in any of the cases, and their means at year 99 differ only by 3×10^{-4} psu from each other.

5. Ocean mean state

The most prominent and robust effects of the diurnal solar cycle are seen in the tropical oceans. Elsewhere, signals tend to be weaker relative to local variability, and hence difficult to extract from the 50-yr integrations. Arguably, the most important equatorial signal is the time-mean SST across the Pacific. In Fig. 3, the model solutions are compared with the observations of Reynolds and Smith (1994). Here, the model SSTs are time mean and averaged between 0.8°S and 0.8°N, and the observational line represents an average between 1°S and 1°N. With the parameterized diurnal cycle in CCSM3, the mean SST is warmer by as much as 1°C compared to C1D, and in much better agreement with observations. The close match of C3H and C1H to CCSM3 indicates that the idealized diurnal cycle performs well, and as far as the ocean is concerned it may not be essential for the atmosphere to receive diurnal SST variability. Unfortunately, CCSM3's poor representation of the seasonal cycle of eastern equatorial Pacific SST anomalies (Large and Danabasoglu 2006) persists in all experiments.

Figure 4 gives the distribution of tropical HBL in CCSM3 compared to C1D, showing that it is about 50% shallower in the central Pacific. Indeed, these differences represent the biggest percentage HBL changes

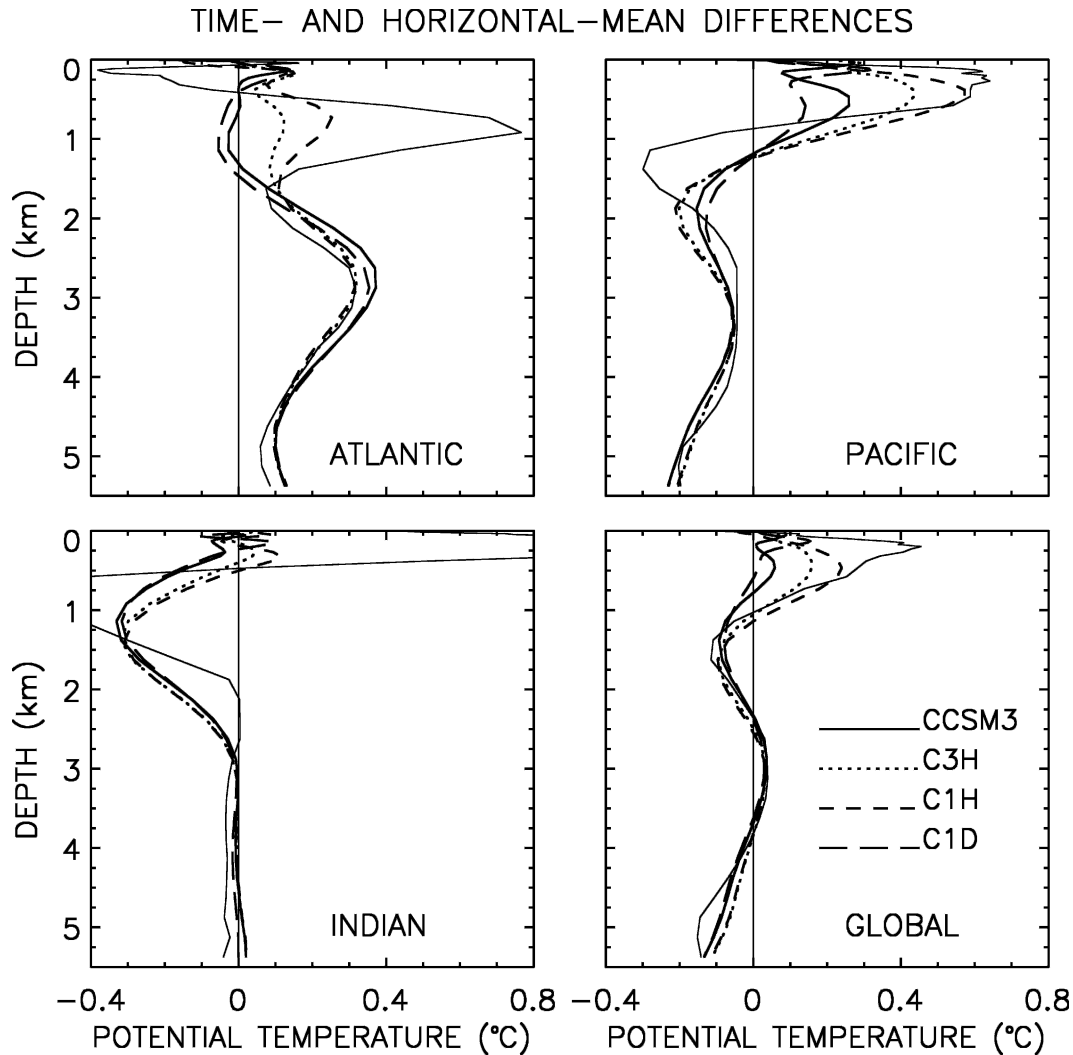## TIME– AND HORIZONTAL–MEAN DIFFERENCES

FIG. 2. Time- and horizontal-mean potential temperature difference profiles. Year 50 means are subtracted from year 95–99 means to compute the differences. The thin solid lines represent the CCSM3 year 50 minus observed climatology difference profiles. For this difference profile, the upper ocean and 1000-m-depth values extend to 1.85° and −0.69°C, respectively, in the Indian Basin.

due to diurnal cycle anywhere on the globe. There are larger absolute changes in the deep water formation regions in the northern North Atlantic. Both C3H and C1H have similar HBL distributions in the equatorial and tropical regions as in CCSM3. In contrast to the equatorial Pacific, HBL significantly deepens especially between 40° and 5°S and between 5° and 40°N in the diurnal cycle cases compared to C1D. This deepening is somewhat spatially uniform, and it is likely due to the dominating effects of nighttime convective mixing. With increased coupling frequency, there is also some deepening of HBL, particularly in the Southern and Arctic Oceans. These increases overwhelm the equatorial decreases as reflected in the global-mean HBL val-
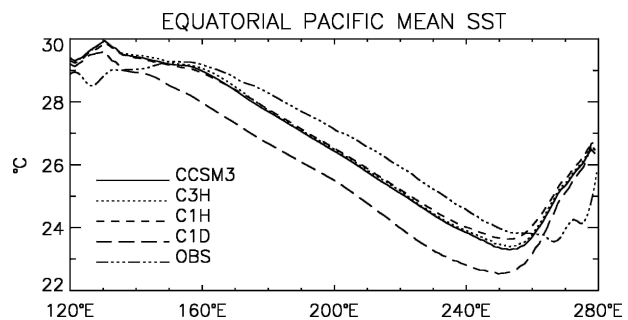

FIG. 3. Equatorial Pacific mean SST. The model solutions are averaged between 0.8°S and 0.8°N and years 80–99. The observational line (OBS) from Reynolds and Smith (1994) is averaged between 1°S and 1°N.
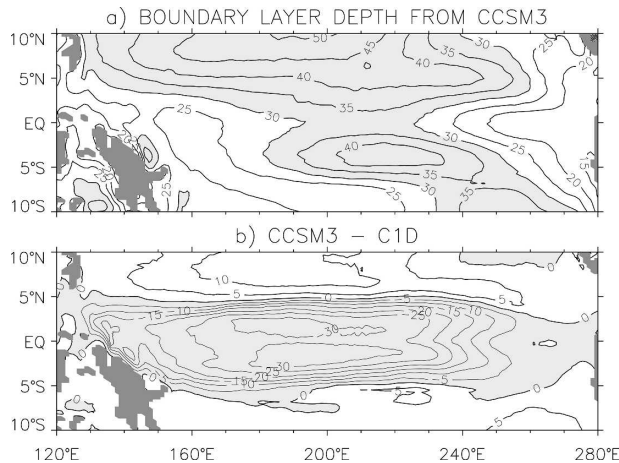
FIG. 4. (a) Time-mean equatorial Pacific boundary layer depth in CCSM3 and (b) its difference from C1D. The contour interval is 5 m in both (a) and (b).

ues of 45.1, 46.8, 49.1, and 50.5 m for C1D, CCSM3, C3H, and C1H, respectively.

In surface heat and freshwater fluxes, some of the largest differences between the diurnal cycle cases and C1D are again confined to the tropical regions, particularly to the west of the date line in the Pacific. As expected, the warmer SSTs lead to less surface heating of the ocean. We compute time-mean surface heat fluxes of about 62.5 and 68.2 W m^{-2} for the diurnal cycle cases and C1D, respectively, for the region 5°S–5°N, 120°–280°E. The net shortwave heat fluxes for the same region are about 214.3 W m^{-2} for the diurnal cycle cases and 216.6 W m^{-2} for C1D, thus accounting for only about 40% of the total heat flux difference. In the far western Pacific, the mean heat flux differences between the diurnal cycle cases and C1D exceed 30 W m^{-2}. These changes are accompanied by more than 30% higher precipitation in the diurnal cycle cases than in C1D (computed for 5°S–5°N, 130°–180°E). However, this additional precipitation does not cause excessive surface freshening that can lead to warmer temperatures and more precipitation through a positive-feedback loop discussed in Large and Danabasoglu (2006) and Yeager et al. (2006), because the central equatorial Pacific SSTs, still colder than observed, appear to be below the threshold for this positive-feedback mechanism. Therefore, the Pacific as well as the Atlantic and Indian EUC strengths and tilts are not substantially different between any of the experiments (not shown). One exception is the slightly shallower (10–15 m) core depths in the Atlantic and Indian basins in C1D. At the surface, the westward flow in the Pacific is stronger by more than 10 cm s^{-1} in C1D compared to

the other cases (not shown). This occurs despite the weaker westward wind stress and can be partially attributed to the changes in the regional momentum balances (Large et al. 2001). The inclusion of the ocean surface velocities in the stress computation may contribute to this weakening of the westward wind stress.

6. Equatorial diurnal rectification

Diurnal cycles in the ocean for CCSM3 and the other experiments are analyzed using the high-frequency sampling over the first five days of each month of year 90. Ensemble means over the 12 months of 5-day time series for temperature, zonal velocity, turbulent momentum flux, and turbulent heat flux are shown in Fig. 5. The most direct effects of the diurnal cycle of solar heating in C1H, C3H, and CCSM3 are the shallow mixed layers and SST warming during the day compared to C1D. Because opposite-signed nighttime signals are quite weak, there is a net diurnal rectification that tends to reduce mean HBL and increase mean SST. To illustrate, diurnal boundary layers in Fig. 5 generally sawtooth between about 20- and 50-m depth, so the daily average HBL is about 35 m. This rectification explains about half the CCSM3 − C1D difference in Fig. 4. The remainder is mostly accounted for by the maximum CCSM3 depth (about 50 m) being about 15 m shallower than C1D HBL. Figure 5 suggests that this bias is due both to the colder and less stratified temperatures of C1D, and to the nighttime deepening being reversed each morning by the stabilizing solar heating before reaching its maximum in CCSM3.

The daytime shallowing of the boundary layer also traps westward (negative) momentum near the surface, leading to a westward acceleration of zonal velocity by about 10 cm s^{-1} in 6 h. Nighttime convective mixing distributes this momentum deeper, which leads to the increase in westward flow at depth in Fig. 5. This diurnal cycle is generated on top of a background of westward surface flow that diminishes with depth and becomes increasingly eastward down to the core of the EUC at 100 m or deeper. Of most importance to vertical mixing is the vertical shear, which is constant in C1D, but diurnally variable in the upper 50 m of the other cases. There is again a rectification effect due to the diurnal cycle, with stronger mean westward surface flow and stronger vertical shear within the boundary layer.

Now suppose, as suggested by Fig. 5, that the SST rises by ΔSST = 0.2°C over the 6 h centered about noon, then falls by the same amount over the next 6 h. The effect on the daily mean SST would be 25% of ΔSST, or 0.05°C. A more precise evaluation of the ef-
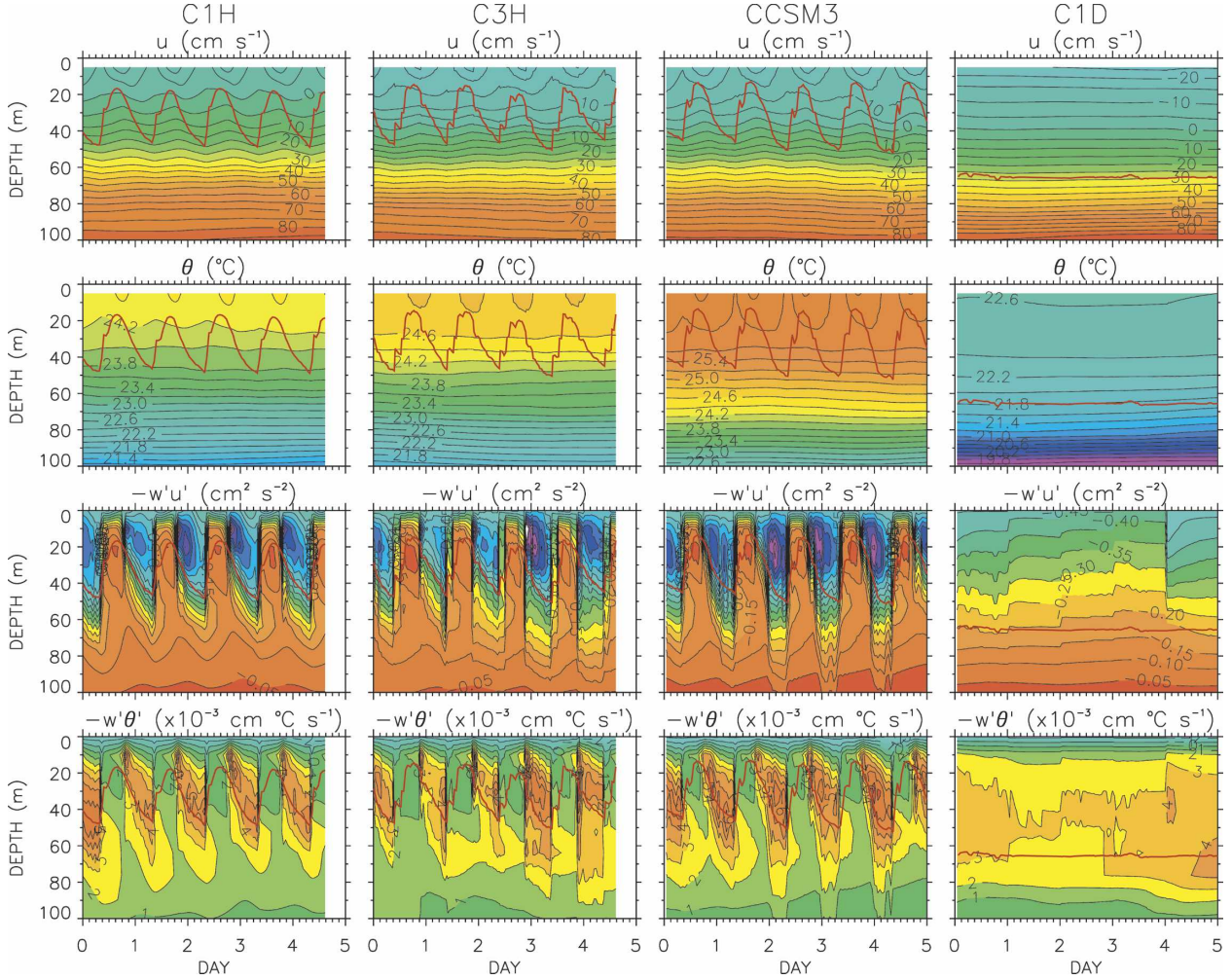
FIG. 5. The 5-day time series of the 12-month ensemble-mean zonal velocity (u), potential temperature (θ), turbulent momentum flux ($-w'u'$), and turbulent heat flux ($-w'\theta'$) obtained on the equator at 140°W for all model experiments. The contour intervals are 5 cm s^{-1}, 0.2°C, 0.05 cm^2 s^{-2}, and 1×10^{-3} cm °C s^{-1}, respectively. The red line indicates the boundary layer depth. The abscissa is in local time, and only the upper 100-m distributions are shown.

fect on mean equatorial SST begins with an evaluation of the temperature stratification anomaly profile,

$$\Delta\theta(d) = \begin{cases} \dfrac{1}{\rho c_p} \displaystyle\int_{\text{DAY}} \dfrac{\text{SHF}(t)}{\text{HBL}(t)} \, dt, & \text{for} \quad d \leq \text{HBL}(t); \\ 0, & \text{for} \quad d > \text{HBL}(t), \end{cases}$$

$$(4)$$

where the ocean transport contributions, exchanges with the ocean interior, and absorption of solar heat flux with depth are excluded. In (4), d is depth from the surface, t is time, and $\rho c_p = 4.1 \times 10^6$ J °C^{-1} m^{-3}. Also, SHF is the surface total heat flux, and both SHF and HBL, which provides the depth dependence of (4), are spatially averaged in the region 0.8°S–0.8°N, 160°–

240°E to capture the primary warming area in the equatorial Pacific. The ensemble-mean profiles for all cases are shown in Fig. 6. Essentially, they are very similar for all diurnal cycle cases, with CCSM3 showing the largest near-surface anomaly, consistent with the larger SST diurnal cycle variation in that case (see below). The negative anomalies below about 25-m depth represent the nighttime cooling of the deeper boundary layer, overcoming the heating due to convective mixing of the warm diurnal mixed layer. In C1D, such anomalies are necessarily absent and the much deeper, well-mixed boundary layer persists without a diurnal cycle.

We can now compute the diurnal cycle rectification on the daily-mean SST in comparison to C1D using

$$\Delta_R \text{SST} = \Delta \text{SST}_{\text{DC}} - \Delta \text{SST}_{\text{C1D}}, \qquad (5)$$
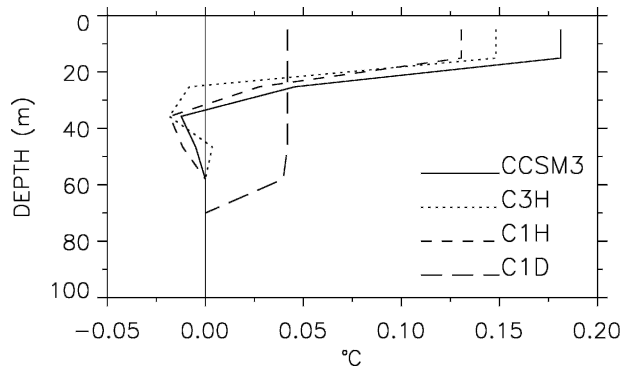
FIG. 6. Temperature stratification anomaly profiles computed using (4).

where DC denotes either C1H, C3H, or CCSM3 and

$$\Delta \text{SST} = \frac{1}{T} \int_{\text{DAY}} \Delta \theta(d=0)\, dt, \qquad (6)$$

with $T = 1$ day. In accord with the above 0.05°C estimate from Fig. 5, we obtain 0.056°, 0.107°, and 0.067°C for C1H, C3H, and CCSM3, respectively. Thus, these rectification effects are very small compared to the 1°C mean SST difference between these cases and C1D (see also Fig. 7) and cannot account for the warmer mean equatorial Pacific SSTs of Fig. 3. However, based on a recent study by Bernie et al. (2005), we note that this small rectified warming and the diurnal cycle of SST (Fig. 5) are underestimated here by as much as a factor of 4 due to the use of model's upper-layer temperature for SST. Using an idealized, one-dimensional model, Bernie et al. (2005) show that a temporal resolution of 3 h or better, which is satisfied by our diurnal cycle cases, and a vertical resolution of 1 m are required to capture 90% of the SST diurnal variability.

The most satisfying result is that the idealized solar diurnal cycle of CCSM3 is very successful at reproducing the diurnal cycle characteristics of C1H, more so even than the less frequent coupling of C3H. This is illustrated by considering the probability distributions of binned 12-h differences in surface zonal velocity (dSSu) and SST (dSST) shown in Fig. 7. These differences are obtained on the equator for the longitude range 137°–143°W for 1800–0600 local time, broadly coinciding with the extrema in all fields. The similarity of the means, standard deviations, and distributions between CCSM3 and C1H is striking, as is the improvement of CCSM3 over C1D. As expected in C1D, the mean values are near zero and the standard deviations are much smaller. The C3H distributions tend to fall between those of C1H and C1D, particularly in their means. This degradation relative to C1H is due to the

3-hourly coupling period, over which the model fluxes are averaged, so that extrema are not as well resolved.

Not unexpected are detailed behaviors that differ between C1H and CCSM3 because local feedbacks are suppressed. For example, as a result of suppressed thermal feedback, the diurnal variation in HBL amplitudes is the largest in CCSM3, mostly due to the shallower minimum depths. Also, SST diurnal cycle of 0.28°C peak to peak in CCSM3 is about 20% higher than in both C1H and C3H. Finally, we note that the differences of over 1°C in upper ocean θ between C1H, C3H, and CCSM3 are due to interannual variability, as demonstrated by the similarity of the long-term averages of SST at this location (Fig. 3).

7. Deep-cycle turbulence

In addition to solar radiation, diurnal variations of equatorial SST are also governed by vertical mixing. There have been extensive ocean observations at the equator (e.g., Gregg et al. 1985; Moum and Caldwell 1985; Lien at el. 1995) of a diurnal cycle of turbulence below the mixed layer. This deep-cycle turbulence has been reproduced in LESs (Wang et al. 1998; Skyllingstad et al. 1999) and one-dimensional vertical mixing parameterization experiments (Large and Gent 1999). The observations have been concentrated near 140°W, so this is also the location of the model results in Fig. 5. The 12-month ensemble averages of the turbulent fluxes of momentum $(-w'u')$ and heat $(-w'\theta')$ over the upper 100 m are shown in the bottom half of the figure. Here, the surface values are the kinematic wind stress and nonsolar heat flux, respectively.

The penetration of the diurnal cycles of θ and zonal velocity is visible down to about 60 m. A robust characteristic of deep-cycle turbulence is that it penetrates far deeper; to 100 m in CCSM3. This turbulence signal becomes rejuvenated by the onset of convection each night, and at least in the model simulations, the stabilizing effect of heat is overcome by the destabilizing shear, so that the turbulence propagates downward below the mixed layer at the diffusive time scale and reaches its maximum depth sometime during the following day. In the meantime, restratification due to daytime solar forcing confines the surface turbulence in a very shallow upper layer that is separated from the deep-cycle turbulence by a minimum in the turbulent fluxes between 20 and 30 m.

All of the diurnal cycle features described above compare very favorably with the existing observations and the related numerical simulations listed above. Of course some differences in detail are expected, with differing surface fluxes and model transports, and the
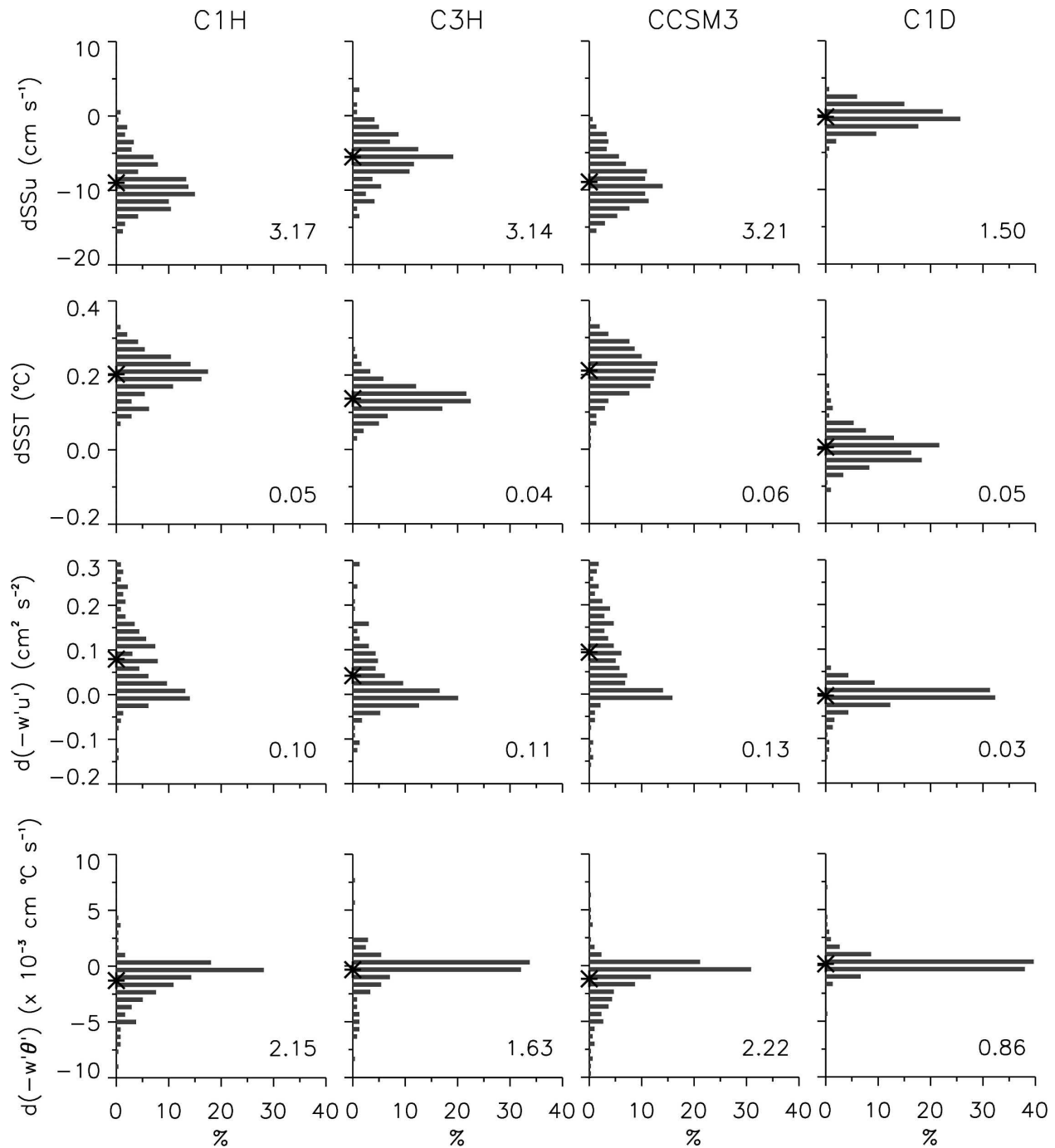
FIG. 7. The 1800−0600 local time binned differences for sea surface zonal velocity (dSSu), SST (dSST), turbulent momentum flux at 1.2HBL$_{max}$ depth [$d(-w'u')$], and turbulent heat flux at 1.2HBL$_{max}$ depth [$d(-w'\theta')$] obtained on the equator for the longitude range 137°–143°W. The bin intervals are 1 cm s^{-1}, 0.02°C, 0.017 cm^2 s^{-2}, and 0.67 × 10^{-3} cm °C s^{-1}, respectively. The bin counts are normalized. In each panel, the means are denoted along the ordinate, and the standard deviations are included.

coarser vertical resolution being possible causes. The latter is likely responsible for the greater daytime boundary layer depths than the 5 m found in Large and Gent (1999). In addition, relative to C1H the onset of convection is delayed by about 3 h, that is, a coupling interval, in C3H, until about 2100 local time. In CCSM3, the onset of convection appears to be less regular, ranging from 1800 to midnight local time.
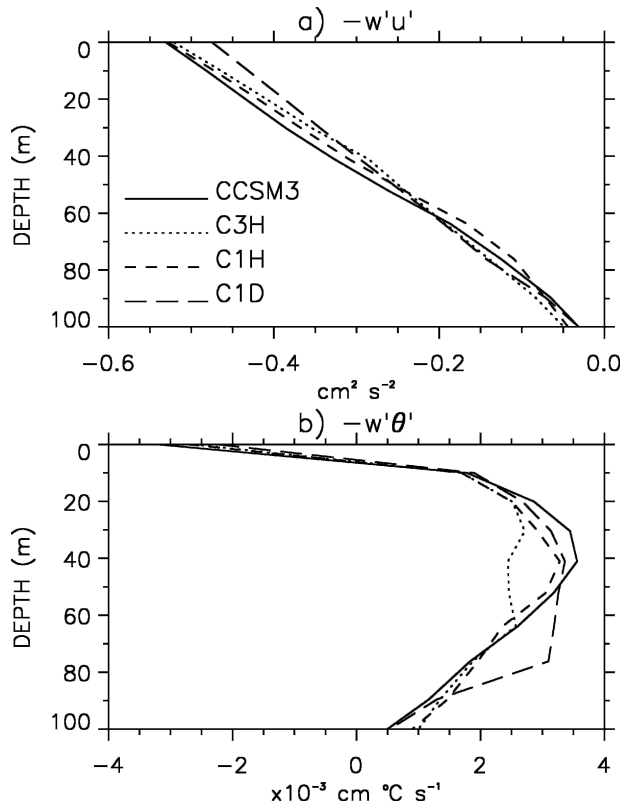
FIG. 8. The 60-day average depth profiles of the turbulent (a) momentum ($-w'u'$) and (b) heat ($-w'\theta'$) fluxes for the upper 100 m on the equator at 140°W.

Large and Gent (1999) attribute these delays to the balance between large shear instability mixing and nighttime surface cooling, without convective deepening.

As an integral measure of the Fig. 5 turbulent fluxes, we show their 60-day mean profiles in Fig. 8. Both fluxes are always approaching zero by 100 m. All cases have very similar momentum flux profiles with negative flux divergences, reflecting the westward acceleration of the prevailing easterly winds. The westward stress is smaller in C1D. In general, there are somewhat larger differences in the turbulent heat flux profiles. As hoped, however, C1H and CCSM3 are more like each other, with their divergences indicating cooling in the upper 40 m and heating below at comparable rates. The C3H profile differs more in the 20–60-m depth range, where the flux divergence is nearly zero. Similarly, there is negligible heating between 40 and 75 m in C1D, but there are rather large flux divergences further down. Figure 8 indicates that the cooling of the upper 40 m due to the divergence of vertical turbulent heat flux is somewhat greater in CCSM3 than in C1D. Therefore, like rectification, vertical heat flux cannot

account for the warmer SSTs in the diurnal cycle cases of Fig. 3.

Finally, we again consider the distributions of 12-h binned differences of Fig. 7, but now focus on the 12-h changes in the turbulent momentum $[d(-w'u')]$ and heat $[d(-w'\theta')]$ fluxes at depth. To highlight the diurnal amplitude variations of deep-cycle turbulence, we subjectively use 1.2 times the maximum daily HBL as the analysis depth. Not only are the average diurnal cycles of fluxes very similar in C1H and CCSM3, but so too are the distributions and standard deviations about the mean. Evidently deep-cycle turbulence is as well represented in CCSM3 as in C1H. With straightforward daily coupling, C1D fails to produce systematic turbulence cycles at depth, and there is only modest improvement in C3H.

8. Role of the atmospheric mean state

The purpose of this section is to explore whether an atmospheric mechanism may lead to the climate mean signal of a warmer equatorial Pacific seen in Fig. 3. To this point, the analysis of the coupled experiments (Table 1) has been unable to fully account for this warming signal, though at least some of the warming can be attributed to rectification (section 6). The remaining fraction of the improvement of the tropical mean state may come about through the mutually cooperative coupled dynamics in the tropical air–sea system, perhaps triggered by the small rectification signal.

To examine, at least qualitatively, such a synergistic relationship between the atmosphere and ocean, it is useful to isolate the atmospheric response to equatorial warming and to identify if any positive feedbacks might be available for the further amplification of the ocean's response to diurnal cycling. A straightforward method of accomplishing this is to use the CAM3 uncoupled simulations, which have been produced for the diagnostic evaluation of the CAM3 climate (Collins et al. 2006a; Hack et al. 2006), by conditionally sampling these integrations during periods of anomalously warm equatorial SSTs (designated as WARM). To do this we have utilized the output for the five warmest years in the 40-yr sample: 1977, 1983, 1987, 1988, and 1997. An analysis of the differences in the equatorial Pacific surface heat fluxes between WARM and the climatology of surface heat fluxes produced in a simulation with climatological monthly SSTs (designated as CONTROL) is performed.

In the equatorial Pacific, the SST differences between WARM and CONTROL (Fig. 9a) is qualita-
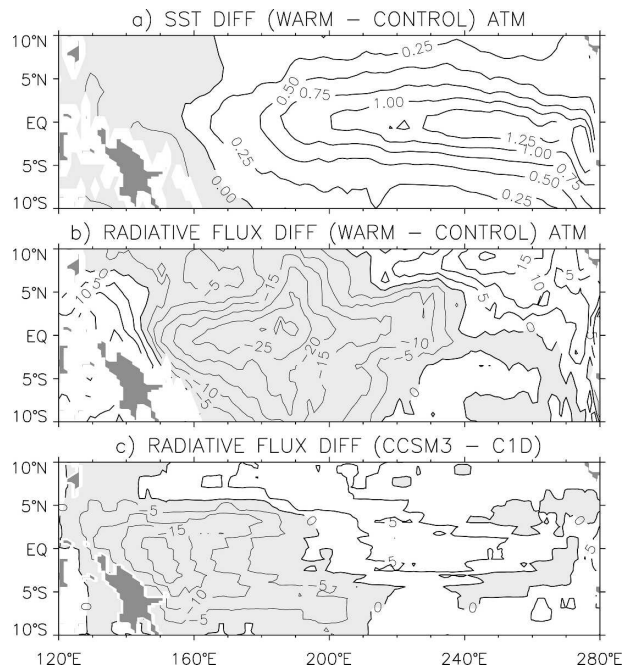
FIG. 9. Annual-mean (a) SST and (b) radiative heat flux differences between the CAM3 integration sampled in warm tropical SST years and a CAM3 control with repeating mean seasonal cycle SSTs and (c) time-mean radiative heat flux difference between CCSM3 and C1D. The contour intervals are 0.25°C and 5 W m^{-2} for the SST and heat flux distributions, respectively, and shading (thin lines) indicates negative differences.

tively very similar to the differences between the diurnal cycle cases and C1D (see Fig. 3) with a fairly broad region of over 1°C warming. We show only the radiative heat flux differences for WARM–CONTROL and CCSM3–C1D in Figs. 9b and 9c, respectively, because the latent and sensible heat flux components act to suppress any warm anomalies in all cases. Both of these difference distributions are dominated by the net short-wave heat flux contributions (not shown). The WARM–CONTROL anomalous fluxes (Fig. 9b) act to reduce the warm SST anomaly. In contrast, in CCSM3–C1D (Fig. 9c), the warm anomaly is reinforced by the positive flux anomalies east of 200°E where more than 15 W m^{-2} positive flux anomaly due to the net short-wave heat flux is partially compensated by the net long-wave component. Moreover, both the magnitude and extent of the negative anomaly region are significantly reduced between 160° and 200°E along the equator because of differences in cloud patterns. These results show that the coupled response is significantly different than in an atmosphere-only integration and that coercive air–sea coupling could be a prime mechanism for amplifying the rectified SST signal to the levels seen in Fig. 3.

9. ENSO variability

In this section, we investigate if the warmer equatorial Pacific SSTs change the ENSO characteristics of the coupled integrations. Figure 10a shows the Niño-3.4 region (5°S–5°N, 170°–120°W) monthly SST anomaly time series from CCSM3 and observations (Smith and Reynolds 1998). Both time series are detrended and smoothed by a 5-point filter, and are from years 50–99 of CCSM3, and 1950–2000 from the observations. The ranges of the two curves are almost the same, and the standard deviation (SD) values are both 0.81°C (Fig. 10b). This is somewhat fortuitous, because the SD values range between 0.6° and 0.9°C if different 50-yr segments from CCSM3 are considered (Yeager et al. 2006). The SD values from the other experiments are shown in Fig. 10b, showing that C1H and C3H SDs are not significantly different from CCSM3. However, C1D has an SD of 1.2°C, which is significantly larger than in CCSM3 or observations.

Figure 10b also shows the power spectra of the Niño-3.4 SST anomalies from the four model experiments and the observations. The observations show a quite broad frequency peak between 3 and 5 yr that is sig-
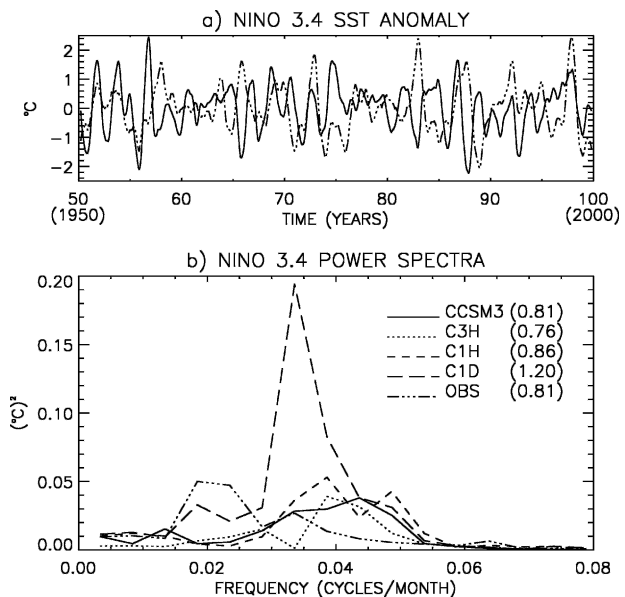

FIG. 10. (a) Smoothed (5 point) and detrended Niño-3.4 monthly SST anomaly time series from CCSM3 and observations (OBS). The respective mean seasonal cycles are subtracted. The CCSM3 and OBS are plotted for model years 50–99 and calendar years 1950–2000, respectively; (b) Niño-3.4 power spectra for CCSM3, C3H, C1H, C1D, and OBS. All time series are processed as above. The Welch window is applied afterward. The bin size is 3. The respective standard deviations for the smoothed and detrended anomaly time series are given in parentheses. See text for significance levels.

nificant at the 99% level. C1D shows a large amplitude peak, reflecting the large SD value, at 2.5 yr. The other cases have power spectra amplitudes that are much more comparable to the observations, but with peaks at even higher frequencies; CCSM3 has a maximum at a period of about 2 yr during this analysis period. Again, all these model peaks are significant at the 99% level.

10. Concluding remarks

The major approximations in the standard air–sea coupling implemented in CCSM3 are that the upper-(lower-) layer ocean (atmosphere) temperature (winds, temperature, and humidity) can be used in surface flux calculations, and that daily coupling combined with an idealized diurnal cycle of solar forcing of the ocean is sufficient. This study evaluates only the latter, and only from the perspective of the ocean simulation. It finds that CCSM3 produces diurnal ocean variability that is nearly identical to cases that resolve the diurnal solar cycle with shorter coupling intervals of 3 h (C3H) and 1 h (C1H). These results represent improvements compared to the previous practice of keeping all ocean forcing, including solar, constant over each day (C1D). For example, essential characteristics of the diurnal cycle of SST, boundary layer depth, zonal velocity, and deep-cycle turbulence are improved in CCSM3 over C1D. Furthermore, the distributions and mean values of 12-h differences for SSTs and the turbulent vertical heat and momentum fluxes obtained at 140°W on the equator agree very well between C1H and CCSM3. This result, and the similarity of ocean mean states, leads to the conclusion that the idealized diurnal cycle of solar forcing in CCSM3 is a valid approach. On the other hand, previous practice, as represented by C1D, produces too much ENSO variability, overly cold equatorial Pacific SSTs, and no diurnal enhancement of the ocean turbulent heat and momentum fluxes associated with deep-cycle turbulence.

Our tropical analysis shows that the most direct effects of the diurnal solar cycle are the expected daytime shoaling of the boundary and mixed layer depths, warming of SST, and surface current acceleration in the direction of the wind. Because opposing nighttime signals are much smaller, there is a net diurnal rectification that tends to reduce the mean boundary layer depth and increase mean SST and westward surface current. This rectification accounts for about half of the reduction in the boundary layer depth. In contrast, a local budget analysis reveals that the rectification of the diurnal heating cycle on the daily mean SST is only 0.05°–0.1°C, much less that the $\approx$1°C reduction in the equatorial Pacific cold bias of C1D. This 1°C reduction

is achieved in both explicit two-way (as in C3H and C1H) and one-way (as in CCSM3) diurnal interaction. A comparison of the surface heat flux differences between CCSM3 and C1D and between atmosphere-only integrations conditionally sampled during periods of anomalously warm equatorial SSTs and a control integration shows a lack of direct atmospheric responses that might be leading to such an amplification. Therefore, it appears that the large-scale air–sea coupling is the prime mechanism in amplifying the rectified SST signals.

The motivation for implementing a simple, conservative diurnal cycle scheme in CCSM3 was to improve the representation of ocean surface forcing within the CCSM3 numerical constraints. The idealized solar cycle has no shortwave heat flux at night, and peaks at 4 times the daily mean value at noon. The peak to peak difference can approach 1000 W m^{-2}, which dwarfs what might be expected from improving the diurnal cycle of SST. The surface heat flux associated with an extreme 2°C SST signal with 2 m s^{-1} winds would be about 14 W m^{-2} when warming and moistening of the lower atmosphere are considered. Nevertheless, the amplification of small SST signals in the coupled system suggests that accounting for cooling and heating of the very near surface of the ocean may produce significant effects on mean SST, which could have broad, large-scale impacts. Although the cases (C1H and C3H), where the atmosphere sees diurnal variability in SST, are very similar to CCSM3 in the ocean, an even more realistic diurnal cycle of SST may cause significant differences in the atmosphere that could project onto the ocean. However, Rasch et al. (2006) report little improvement in CAM3 variability when subdiurnal time scales are resolved in the surface properties, likely due to problems with the atmospheric convective parameterization. Local responses are also unlikely to improve equatorial Pacific SSTs, because the model SST is already too warm west of 150°E (Fig. 3), and farther east where the cold bias is still large, the necessary low winds are less frequent, at least in CCSM3. In addition to an improved SST, an overall assessment of the importance of the diurnal cycle will also require that other coupling issues be confronted, such as finer upper-ocean resolution, the $\approx$60-m atmospheric winds, temperature, and humidity in the low-wind conditions favorable to a large diurnal cycle, a global treatment of gustiness, and the SST–radiation time shift.

We find that the inclusion of an idealized diurnal cycle of solar forcing within the ocean model does not alter the ocean model's global cooling trend, a persistent feature of the past and present CCSM control integrations. In contrast, this cooling trend can be elimi-

nated or even reversed when the atmospheric model feels the SST diurnal cycle through more frequent ocean coupling. Unfortunately, this trend reversal, that is, warming, may not even be desirable, because it occurs within the upper 1000 m globally, where the ocean is already too warm compared to observations. Longer integrations are required to determine if these trend changes are robust features.

Finally, we note that our idealized diurnal cycle is independent of longitude and that everywhere the length of day is 12 h every day of the year. This is geared toward the Tropics where the diurnal cycle is the largest. These shortcomings can be remedied in the future, but doing so is unlikely to change the solutions in the Tropics where CCSM3 already successfully reproduces the mean and diurnal cycle properties of C1H in which the diurnal solar cycle is explicitly resolved.

APPENDIX A

Modifications to the KPP

This appendix describes the CCSM3 modifications to the KPP vertical mixing parameterization of Large et al. (1994, hereafter LMD). The primary motivation behind these changes is to produce deeper, more realistic, mixed layer depths. The strategy is to make the CCSM3 implementation more consistent with the LMD development, to improve the physical basis, to formulate the numerics to take advantage of oceanic structure, and to remove troublesome pathologies. The most important function of KPP is the diagnosis of boundary layer depth, HBL, from a profile of bulk Richardson numbers, Rb_k, computed at the depth, d_k, of each grid level:

$$Rb_k = \frac{(B_r - B_k)d_k}{|\mathbf{V}_r - \mathbf{V}_k|^2 + V_t^2}, \quad (A1)$$

where B_k (B_r) and $\mathbf{V}_k(\mathbf{V}_r)$ are the level k (near-surface reference) buoyancy and velocity, respectively, while V_t is parameterized turbulent shear. The depth where Rb first reaches a critical value, $Ri_c = 0.3$, is HBL.

In our B-grid implementation, Rb is computed at the T-grid points and previously the resolved shear squared, $|\mathbf{V}_r - \mathbf{V}_k|^2$, was taken as the average over the four neighboring horizontal velocity points. In order for HBL to better represent the maximum vertical penetration of turbulent boundary layer eddies anywhere in a grid cell, this shear is now taken to be the maximum from these four velocity points. The larger shear reduces each Rb_k and hence increases HBL, but typically only by 1–2 m.

Since B_r, B_k, and d_k are all well defined, the only other way of decreasing Rb is to increase

$$V_t^2 = \gamma C_v Ri_c^{-1} d_k N w_s, \quad (A2)$$

where γ is a constant defined by LMD. In LMD, the above buoyancy frequency, N, is that of the interior below HBL. Therefore, it is now based on the density differences between levels k and $k + 1$, instead of between $k - 1$ and $k + 1$, and hence is generally greater. The turbulent velocity scale, w_s, usually equals the friction velocity at the surface and increases in unstable forcing over the uppermost 10% of the boundary layer, then is held constant below in order to avoid excessively large values as depth increases. For consistency, a similar constraint is now applied in stable forcing that limits the decrease in w_s with depth, and hence increases V_t. The effectiveness of these two increases is severely limited by the physical constraint that in pure convection the entrainment buoyancy flux should be 20% of surface flux, which is enforced by empirically determining C_v. As N and w_s are increased, C_v tends to decrease. Conceptually, C_v is the ratio of the interior N to the buoyancy frequency at the entrainment depth and until now has been set to 1.8. However, a series of experiments for our CCSM3 implementation suggests a dependency on N, particularly for small N:

$$C_v = \begin{cases} 2.1 - 200N, & \text{for } N \leq 0.002\text{s}^{-1}; \\ 1.7, & \text{otherwise.} \end{cases} \quad (A3)$$

In total, all the modifications to the computation of V_t increase the overall HBL by only a few meters.

Far more effective at deepening HBL is a change from linear to quadratic interpolation for determining HBL. The systematic shallow bias resulting from linear interpolation is shown in LMD and reproduced in Fig. A1. Here, idealized buoyancy and velocity profiles are assumed to give a profile of Rb with Rb = 0 down to a mixed layer depth of hmix, and increasing incrementally by 0.3 (= Ri_c) every 2 m below, so that HBL (thin solid line) is always 2 m deeper than hmix. As hmix
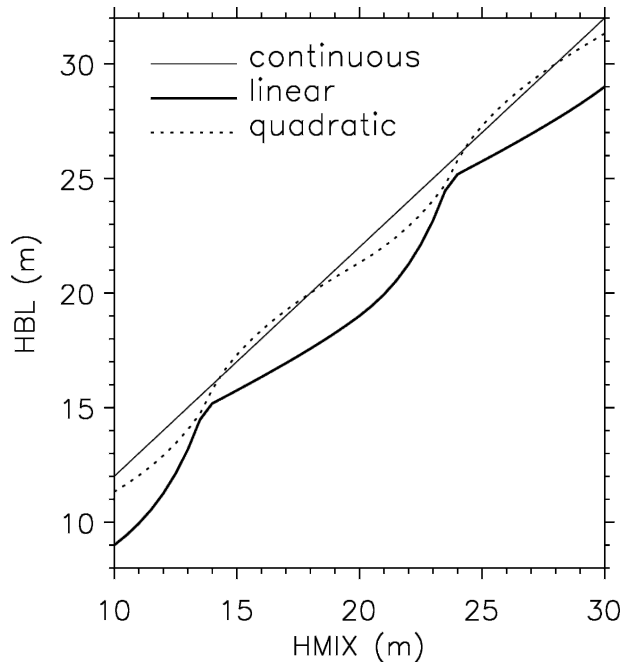
FIG. A1. Evolution of the boundary layer depth (HBL) as the mixed layer (hmix) deepens from 10- to 30-m depth through two vertical grid cells; from idealized continuous equations with HBL = hmix + 2 m, and from linear and quadratic interpolation of the discretization.
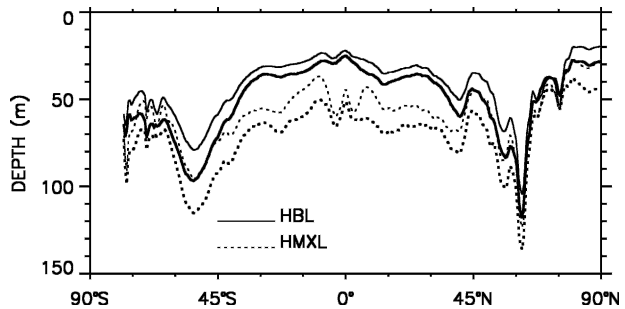

FIG. A2. Global-, time- and zonal-mean boundary (HBL) and mixed layer (HMXL) depths from quadratic CCSM3 (thick lines) and linear interpolation (thin lines).

increases through a discrete grid with 10-m spacing, the discrete Rb_k are taken as averages over the grid cell. Linear interpolation between $Rb_k < Ri_c$ and $Rb_{k+1} > Ri_c$ below gives HBL (thick solid line) that is always less than continuous (thin solid line) by an amount that oscillates depending on the positioning of hmix within the grid. The alternative quadratic interpolation recognizes that oceanic properties tend to be linear, if not constant, in the mixed layer. Therefore, a unique quadratic is found from the values Rb_k and Rb_{k+1}, and the slope at depth d_k defined by Rb_{k-1} and Rb_k. The resulting HBL (dotted trace) is now sometimes greater than continuous, always deeper than linear, and less oscillatory. These improvements become more dramatic as the grid spacing increases, as it does with depth in CCSM3.

To demonstrate the impacts of interpolation in coupled simulations, the first 15 yr of CCSM3 was repeated using linear interpolation. Figure A2 compares HBL and mixed layer depth (HMXL), a stability-based characterization of upper-ocean structure (Large et al. 1997) that is usually greater than hmix and HBL. The zonal-mean and time-averaged (for years 6–15) global distributions show an overall deepening of both measures. Deeper values of more than 10 m are common, with the largest increases of more than 30 m occurring

in the Southern Ocean. The global-mean values for HBL and HMXL in quadratic CCSM3 are deeper than the linear case by 7.5 and 12.4 m, respectively.

A rare pathology is the occurrence of static instability ($N < 0$) just below the boundary layer. The resulting large interior mixing coefficients can lead to unphysical behavior when interior and boundary layer mixing are being matched. Therefore, interior convection is now diagnosed only after the KPP boundary layer and other interior mixing profiles have been determined. Another pathology is avoided by only using positive values of the discriminant in the above quadratic interpolation.

The salt diffusivity (κ_S) for the salt fingering regime of double-diffusive mixing has been modified to reflect the recent observational estimates (St. Laurent and Schmitt 1999) and direct numerical simulations. It is now given by

$$\kappa_S = \kappa_o \left[1 - \left(\frac{R_\rho - 1}{2.55 - 1} \right)^3 \right], \qquad (A4)$$

where R_ρ is the double-diffusion density ratio, and at $R_\rho = 1$, the maximum value of $\kappa_o (=1.0 \times 10^{-4} \text{ m}^2 \text{ s}^{-1})$ is 10 times smaller than in LMD. The falloff with increasing R_ρ is quite sharp, which limits the effects of double diffusion (Merryfield et al. 1999). Therefore, in a 15-yr sensitivity experiment, the model solutions with no double diffusion differ very little from those of CCSM3. For example, the global- and time-mean HBL and HMXL are shallower by only about 0.2 m without the double-diffusive mixing.

The Ekman and Monin–Obukhov depth computations are rewritten to include only the shortwave radiation absorbed in HBL. These limits can be enforced under stable forcing conditions, but this is not done in our standard implementation. We also use a single pass of a Laplacian filter on HBL to attenuate some two-grid-point spatial noise.
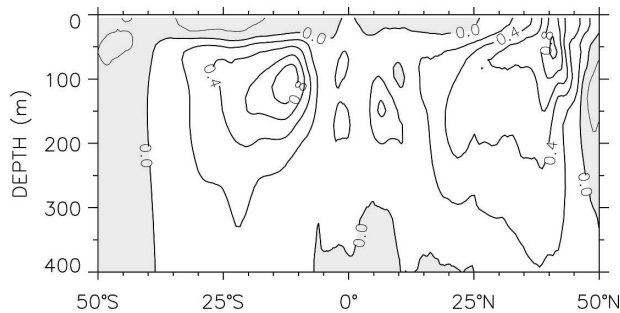
FIG. B1. Global-, time- and zonal-mean potential temperature difference distributions; CCSM3 minus constant Jerlov Type IB absorption. The contour interval is 0.2°C, and shading (thin lines) indicates negative differences.

APPENDIX B

Spatially Varying, Monthly Solar Absorption

The absorption of solar radiation in the upper ocean is based on spatially varying, monthly climatologies of chlorophyll inferred from a limited set of satellite ocean color data, spanning the period from September 1997 to November 2001 (Ohlmann 2003). There is a surface absorption and a double-exponential transmission of the remainder, based on empirical fits to atmospheric–oceanic radiative transfer model calculations, validated against in situ radiation and biological data. Chlorophyll is assumed to be uniformly distributed in the vertical. In our present implementation, the transmission coefficients are updated once a month. Compared to the spatially and temporally constant Jerlov Type IB transmission in CCSM2, where the double exponential of Simpson and Paulson (1979) is used, small chlorophyll amounts (from the minimum 0.01 to 0.2 mg m^{-3}) result in less near-surface absorption and more at depth, while the larger chlorophyll amounts (>0.3 mg m^{-3}) have more near-surface absorption and less at depth. The mean chlorophyll distribution shows distinct regimes of low amounts in subtropical gyre centers (0.03 to 0.07 mg m^{-3}) and enhanced amounts along the equator and near coasts (0.3 to 0.6 mg m^{-3} or larger).

In ocean-only sensitivity experiments, the global values of absorbed flux with the new formulation show a decrease in surface layer solar absorption of order 12 W m^{-2} and a corresponding enhancement at depth compared to the Jerlov Type IB transmission. However, there is considerable regional variation. A coupled sensitivity experiment was performed by reintegrating the first 15 yr of CCSM3 using the Jerlov Type IB transmission. The major impacts of the new formulation are evident in the upper 400-m zonal-mean potential temperature differences of Fig. B1. Here, the global differ-

ences are based on the time-mean distributions for years 6–15. The tropical and subtropical upper-ocean waters show broad warming below the surface, locally exceeding 0.8°C, and a corresponding surface cooling of about 0.2°C. This destabilizing effect is accompanied by deepening of the boundary layer by about 5 m on average. The equatorial and coastal warming signals of about 0.3°C in SST present in the ocean-only experiments with this new formulation (not shown) are too anemic to be detected above any SST changes associated, in particular, with ENSO variability in coupled experiments.

REFERENCES

Anderson, S. P., R. A. Weller, and R. B. Lukas, 1996: Surface buoyancy forcing and the mixed layer of the western Pacific warm pool: Observations and 1D model results. *J. Climate,* **9,** 3056–3085.

Bernie, D. J., S. J. Woolnough, J. M. Slingo, and E. Guilyardi, 2005: Modeling diurnal and intraseasonal variability of the ocean mixed layer. *J. Climate,* **18,** 1190–1202.

Bourassa, M., D. G. Vincent, and W. L. Wood, 1999: A flux parameterization including the effects of capillary waves and sea state. *J. Atmos. Sci.,* **56,** 1123–1139.

Bradley, E. F., 1968: A shearing stress meter for micrometeorological studies. *Quart. J. Roy. Meteor. Soc.,* **94,** 380–387.

Briscoe, M. G., and R. A. Weller, 1984: Preliminary results from the Long Term Upper-Ocean Study (LOTUS). *Dyn. Atmos. Oceans,* **8,** 243–265.

Brunke, M. A., X. Zeng, and S. Anderson, 2002: Uncertainties in sea surface turbulent flux algorithms and data sets. *J. Geophys. Res.,* **107,** 3141, doi:10.1029/2001JC000992.

Bryan, F. O., B. G. Kauffman, W. G. Large, and P. R. Gent, 1996: The NCAR CSM flux coupler. NCAR Tech. Note NCAR/TN-424+STR, 50 pp. [Available online at http://www.ccsm.ucar.edu/models/cpl/doc3/index.html.]

Bryan, K., 1969: A numerical method for the study of the circulation of the world ocean. *J. Comput. Phys.,* **4,** 347–376.

Collins, W. D., and Coauthors, 2006a: The formulation and atmospheric simulation of the Community Atmosphere Model version 3 (CAM3). *J. Climate,* **19,** 2144–2161.

——, and Coauthors, 2006b: The Community Climate System Model: CCSM3. *J. Climate,* **19,** 2122–2143.

Deser, C., and C. A. Smith, 1998: Diurnal and semidiurnal variations of the surface wind field over the tropical Pacific ocean. *J. Climate,* **11,** 1730–1748.

Doney, S. C., W. G. Large, and F. O. Bryan, 1998: Surface ocean fluxes and water-mass transformation rates in the coupled NCAR climate system model. *J. Climate,* **11,** 1420–1441.

Dukowicz, J. K., and R. D. Smith, 1994: Implicit free-surface formulation of the Bryan-Cox-Semtner ocean model. *J. Geophys. Res.,* **99,** 7991–8014.

Fairall, C. W., E. F. Bradley, J. S. Godfrey, G. A. Wick, J. B. Edson, and G. S. Young, 1996a: Cool-skin and warm-layer effects on sea surface temperature. *J. Geophys. Res.,* **101,** 1295–1308.

——, ——, D. P. Rogers, J. B. Edson, and G. S. Young, 1996b: Bulk parameterization of air-sea fluxes for Tropical Ocean-

Global Atmosphere Coupled-Ocean Atmosphere Response Experiment. *J. Geophys. Res.,* **101,** 3747–3764.

——, ——, J. E. Hare, A. A. Grachev, and J. B. Edson, 2003: Bulk parameterization of air–sea fluxes: Updates and verification for the COARE algorithm. *J. Climate,* **16,** 571–591.

Gent, P. R., and J. C. McWilliams, 1990: Isopycnal mixing in ocean circulation models. *J. Phys. Oceanogr.,* **20,** 150–155.

Gregg, M. C., H. Peters, J. C. Wesson, N. S. Oakey, and T. J. Shay, 1985: Intensive measurements of turbulence and shear in the equatorial undercurrent. *Nature,* **318,** 140–144.

Griffies, S. M., 1998: The Gent–McWilliams skew flux. *J. Phys. Oceanogr.,* **28,** 831–841.

Hack, J., J. Caron, S. Yeager, M. Holland, K. Oleson, A. Dai, J. Truesdale, and P. Rasch, 2006: Simulation of the global hydrological cycle in the CCSM Community Atmosphere Model version 3: Mean features. *J. Climate,* **19,** 2199–2221.

Holtslag, A. A. M., and B. A. Boville, 1993: Local versus nonlocal boundary-layer diffusion in a global climate model. *J. Climate,* **6,** 1825–1842.

Kauffman, B. G., R. Jacob, T. Craig, and W. G. Large, cited 2004: The CCSM Coupler version 6.0: User's guide, source code reference, and scientific description. [Available online at http://www.ccsm.ucar.edu/models/ccsm3.0/cpl6/users_guide/users_guide.html.]

Kawai, Y., and H. Kawamura, 2002: Evaluation of the diurnal warming of sea surface temperature using satellite-derived marine meteorological data. *J. Oceanogr.,* **58,** 805–814.

Kiehl, J. T., and P. R. Gent, 2004: The Community Climate System Model, version 2. *J. Climate,* **17,** 3666–3682.

Komen, G. J., L. Cavaleri, M. Donelan, K. Hasselmann, S. Hasselmann, and P. A. E. M. Janssen, 1994: *Dynamics and Modelling of Ocean Waves.* Cambridge University Press, 532 pp.

Large, W. G., and S. Pond, 1981: Open ocean momentum flux measurements in moderate to strong winds. *J. Phys. Oceanogr.,* **11,** 324–336.

——, and P. R. Gent, 1999: Validation of vertical mixing in an equatorial ocean model using large eddy simulations and observations. *J. Phys. Oceanogr.,* **29,** 449–464.

——, and S. G. Yeager, 2004: Diurnal to decadal global forcing for ocean and sea-ice models: The data sets and flux climatologies. NCAR Tech. Note NCAR/TN-460+STR, 105 pp. [Available online at http://www.cgd.ucar.edu/oce/pubs/04pubs.html.]

——, and G. Danabasoglu, 2006: Attribution and impacts of upper-ocean biases in CCSM3. *J. Climate,* **19,** 2325–2346.

——, J. C. McWilliams, and S. C. Doney, 1994: Oceanic vertical mixing: A review and a model with a nonlocal boundary layer parameterization. *Rev. Geophys.,* **32,** 363–403.

——, G. Danabasoglu, S. C. Doney, and J. C. McWilliams, 1997: Sensitivity to surface forcing and boundary layer mixing in a global ocean model: Annual-mean climatology. *J. Phys. Oceanogr.,* **27,** 2418–2447.

——, ——, J. C. McWilliams, P. R. Gent, and F. O. Bryan, 2001: Equatorial circulation of a global ocean climate model with anisotropic horizontal viscosity. *J. Phys. Oceanogr.,* **31,** 518–536.

Ledwell, J. R., E. Montgomery, K. Polzin, L. St. Laurent, R. Schmitt, and J. Toole, 2000: Evidence for enhanced mixing over rough topography in the abyssal ocean. *Nature,* **403,** 179–182.

Levitus, S., T. Boyer, M. Conkright, D. Johnson, T. O'Brien, J.

Antonov, C. Stephens, and R. Gelfeld, 1998: *Introduction.* Vol. 1, *World Ocean Database 1998,* NOAA Atlas NESDIS 18, 346 pp.

Lien, R. C., D. R. Caldwell, M. C. Gregg, and J. N. Moum, 1995: Turbulence variability at the equator in the central Pacific at the beginning of the 1991–1993 El Niño. *J. Geophys. Res.,* **100,** 6881–6898.

Magnusdottir, G., C. Deser, and R. Saravanan, 2004: The effects of North Atlantic SST and sea ice anomalies on the winter circulation in COM3. Part I: Main features and storm track characteristics of the response. *J. Climate,* **17,** 857–876.

Merryfield, W. J., G. Holloway, and A. E. Gargett, 1999: A global ocean model with double-diffusive mixing. *J. Phys. Oceanogr.,* **29,** 1124–1142.

Moum, J. N., and D. R. Caldwell, 1985: Local influences on shear-flow turbulence in the equatorial ocean. *Science,* **230,** 315–316.

Ohlmann, J. C., 2003: Ocean radiant heating in climate models. *J. Climate,* **16,** 1337–1351.

Rasch, P. J., M. J. Stevens, L. Ricciardulli, A. Dai, R. Wood, B. Boville, B. Eaton, and J. J. Hack, 2006: Characterization of tropical transient activity in the CAM3 atmospheric hydrologic cycle. *J. Climate,* **19,** 2243–2266.

Reynolds, R. W., and T. M. Smith, 1994: Improved global sea surface temperature analyses using optimum interpolation. *J. Climate,* **7,** 929–948.

Schudlich, R. R., and J. R. Price, 1992: Diurnal cycles of current, temperature and turbulent dissipation in a model of the equatorial upper ocean. *J. Geophys. Res.,* **97,** 5409–5422.

Simpson, J. J., and C. A. Paulson, 1979: Mid-ocean observations of atmospheric radiation. *Quart. J. Roy. Meteor. Soc.,* **105,** 487–502.

Skyllingstad, E. D., W. D. Smyth, J. N. Moum, and H. Wijesekera, 1999: Upper-ocean turbulence during a westerly wind burst: A comparison of large-eddy simulation results and microstructure measurements. *J. Phys. Oceanogr.,* **29,** 5–28.

Smagorinsky, J., 1993: Some historical remarks on the use of nonlinear viscosities. *Large Eddy Simulation of Complex Engineering and Geophysical Flows,* B. Galperin and S. A. Orszag, Eds., Cambridge University Press, 3–36.

Smith, R. D., and P. R. Gent, 2002: Reference manual for the Parallel Ocean Program (POP), ocean component of the Community Climate System Model (CCSM2.0 and 3.0). Los Alamos National Laboratory Tech. Rep. LA-UR-02-2484, 75 pp. [Available online at http://www.ccsm.ucar.edu/models/ccsm3.0/pop.]

——, and J. C. McWilliams, 2003: Anisotropic horizontal viscosity for ocean models. *Ocean Modell.,* **5,** 129–156.

——, J. K. Dukowicz, and R. C. Malone, 1992: Parallel ocean general circulation modeling. *Physica D,* **60,** 38–61.

——, S. Kortas, and B. Meltz, 1995: Curvilinear coordinates for global ocean models. Los Alamos National Laboratory Tech. Rep. LA-UR-95-1146, 38 pp.

Smith, T. M., and R. W. Reynolds, 1998: A high-resolution global sea surface temperature climatology for the 1961–90 base period. *J. Climate,* **11,** 3320–3323.

Steele, M., R. Morley, and W. Ermold, 2001: PHC: A global ocean hydrography with a high-quality Arctic Ocean. *J. Climate,* **14,** 2079–2087.

St. Laurent, L., and R. W. Schmitt, 1999: The contribution of salt

fingers to vertical mixing in the North Atlantic tracer release experiment. *J. Phys. Oceanogr.,* **29,** 1404–1424.

Stuart-Menteth, A. C., I. S. Robinson, and P. G. Challenor, 2003: A global study of diurnal warming using satellite-derived sea surface temperature. *J. Geophys. Res.,* **108,** 3155, doi:10.1029/2002JC001534.

Wang, D., J. C. McWilliams, and W. G. Large, 1998: Large-eddy simulation of the diurnal cycle of deep equatorial turbulence. *J. Phys. Oceanogr.,* **28,** 129–148.

Webster, P. J., C. A. Clayson, and J. A. Curry, 1996: Clouds, radiation, and the diurnal cycle of sea surface temperature in the tropical western Pacific. *J. Climate,* **9,** 1712–1730.

WGASF, 2000: Intercomparison and validation of ocean-atmosphere energy flux fields. *Joint WCRP/SCOR Working Group on Air-Sea Fluxes,* P. K. Taylor, Ed., WCRP-112, WMO Tech. Doc. 1036, 306 pp.

Yeager, S. G., J. J. Hack, C. A. Shields, and W. G. Large, 2006: The low-resolution CCSM3. *J. Climate,* **19,** 2545–2566.